ORIGINAL ARTICLE

Room-temperature fabrication of magnetite-boehmite sol-gel composites for heavy metal ions removal

Olga E. Shapovalova, Andrey S. Drozdov [*], **Ekaterina A. Bryushkova, Maxim I. Morozov, Vladimir V. Vinogradov**

Laboratory of Solution Chemistry of Advanced Materials and Technologies, ITMO University, Lomonosova st. 9, St. Petersburg 197101, Russian Federation

Abstract Magnetite-boehmite porous ceramic composites were synthesized from magnetite and boehmite hydrosols in a course of room-temperature sol-gel transition. The proposed synthesis routine allowed producing ceramic matrices with a high degree of structure homology, realizing the full range of composites combining magnetite and boehmite phases at any mass ratio. Depending on the magnetite to boehmite ratio the total surface area of the composites can be varied from 122 to 391 m^2/g while the magnetization of the composites can reach up to 88 emu/g. The synthesized composites were examined as adsorbent for Cr(VI) ions and showed the pseudo-second order sorption kinetics. The characterized adsorption behavior was in best accord with the Langmuir model, showing the maximum adsorption capacities of Cr(VI) ions up to 62.4 mg/g. Owing to their magnetic properties the magnetite-containing composites can be magnetically separated and reused for up to 5 times with only minor drop to the sorption capacity down to 89% of its initial value. These make the magnetite-boehmite composites prospective for various applications, including wastewater treatment.

© 2018 Production and hosting by Elsevier B.V. on behalf of King Saud University. This is an open access article under the CC BY-NC-ND license (http://creativecommons.org/licenses/by-nc-nd/4.0/).

1. Introduction

Contamination of water with heavy metal ions is one of essential environmental issues that concern the safety of aquatics. Heavy metal ions are released into the aquatic environment in a variety of industrial processes, such as electroplating, metal processing, dying with inorganic pigments, etc. (Mohan and Pittman, 2006; Wu et al., 2012). Among them, hexavalent chromium Cr(VI) is one of the most dangerous pollutants in wastewater. High toxicity of hexavalent chromium is

due to its strong oxidizing properties, which may irritate biological tissues and result in carcinogenic and mutagenic effects (Uysal and Ar, 2007; Dayan and Paine, 2001). Materials containing Cr(VI) ions are widely used for preparation of a great variety of industrial products, such as pigments for the manufacture of paints, inks, rubber, ceramics, corrosion inhibitors, fungicides, etc. with the total chrome consumption reaching 13 millions tons per year (Idachaba et al., 2004; Saha et al., 2011). Accordingly the guideline of the Whorld Health Organization (WHO) the maximum allowable limit of total chromium in drinking water is only 0.05 mg/dm^3 (Guidelines for Drinking-water Quality Recommendations, 2004). Nonetheless, this limit is often exceeded due to poor treatment of industrial effluents, especially in developing countries with intense heavy industry. Thus, an enhancement of efforts in developing new cost-efficient materials and methods of wastewater treatment becomes inevitable (Pellerin and Booker, 2000; Calder, 1988). Numerous studies concerning removal of Cr(VI) ions from its aqueous solutions have been carried out. The main strategies include purification by coagulation processes with subsequent separation of solid phases (Yao et al., 2017; Liu et al., 2017; Sun and Huang, 2002; Wang et al., 2017), reduction of hexavalent chromium to trivalent state with subsequent separation (Ölmez, 2009; Lakshmipathiraj et al., 2008; Qin et al., 2005), membrane filtration (Kozlowski and Walkowiak, 2002; Goyal et al., 2011; Owlad et al., 2009) and removal by adsorption onto various materials. The latter one gained the most attention due to high efficiency and broad technological diversity, especially when combined with appropriate regeneration cycles (Wang et al., 2017a; Dakiky et al., 2002). In the past years, much attention was paid to the nanostructured adsorbents with highly developed surface area and sorption capacity. The variety of nanoadsorbent materials ranges from activated carbon (Deng et al., 2015; Ihsanullah et al., 2016), carbon nanotubes (Abbas et al., 2016; Qureshi et al., 2017), polyelectrolytes (Ahmad et al., 2015; Gao et al., 2014), to metal oxides (Krivoshapkin et al., 2015; Mikhaylov et al., 2017; Pandey and Tripathi, 2017; Gallios et al., 2017), magnetic nanoparticles (Zeng et al., 2014; Legaria et al., 2015; Keyhanian et al., 2016; Karimi and Kafi, 2015) and their mixtures in all possible combinations (Wang et al., 2017a,b; Zhu et al., 2017; Song et al., 2017a,b). Special attention was paid to various sol-gel derived materials due to their cost-efficient processing, high sorption capacity and stability, as well as possibility to control properties by variation of composition and the synthesis conditions (Zeng et al., 2014; Ciesielczyk et al., 2014, 2017; Camacho et al., 2010; Yang et al., 2006). For instance, introduction of magnetic nanoparticles into sol-gel composites makes them magnetically separable, which simplifies recycling and regeneration of the adsorbent (Zeng et al., 2014; Zhang et al., 2006, 2013; He et al., 2014; Huang and Hu, 2008). The most known magnetic sol-gel adsorbents are based on silica matrix modified with magnetite nanoparticles, while other magnetic sol-gel composites are much less studied. In this work, we are shifting the attention to another class of sol-gel derived materials based on alumina (boehmite) as the high-surface area former known for high chromium sorption capacities (Aide and Cummings, 1997; Granados-Correa and Jiménez-Becerril, 2009) and ferria (magnetite) as the magnetic inclusion. The choice of these components was favored by the following advantages: simplicity and cost-efficiency of synthesis, excellent colloidal stability of

hydrosols, and capability to undergo irreversible sol-gel transition at room temperature with formation of rigid mesoporous ceramic matrices (Chapurina et al., 2016; Drozdov et al., 2016). These two oxides can be mixed at an appropriate ratio supporting highly homogeneous colloid solution. Additionally, this ratio affects the properties of the corresponding composite ceramic matrices, such as specific surface area, absorption capacity or magnetization, and thus can be controlled in a wide range in order to meet the requirements for specific tasks and applications. The relationships between the alumina-to-ferria ratio, physicochemical properties, and absorption capacities of the sol-gel derived composites are discussed.

2. Experimental details

2.1. Chemicals

Aluminum isopropoxide $\geqslant 99\%$, iron(II) chloride tetrahydrate $\geqslant 98.5\%$, iron(III) chloride hexahydrate $\geqslant 99\%$, aqueous solution of ammonia $\geqslant 27.5\%$, potassium bichromate, hydrochloric acid, sodium hydroxide were obtained from Sigma-Aldrich.

2.2. Ferria hydrosol

Stable ferria hydrosol was prepared in a manner described in our previous work (Drozdov et al., 2016; Shabanova et al., 2016) and illustrated in Scheme 1a. 2.5 g FeCl$_2$*4H$_2$O and 5 g FeCl$_3$*6H$_2$O were dissolved in 100 mL of deionized water under constant stirring (500 rpm). Then, 12 mL of aqueous ammonia solution was added under constant stirring (500 rpm) at room temperature. Formed magnetite precipitate was magnetically separated and washed with deionized water until neutral pH. The washed black precipitate was mixed with 100 mL of deionized water and subjected to ultrasonic treatment (37 kHz, 110 W) under constant stirring (300 rpm). The resulting magnetite sol was afterwards cooled to room temperature. The resulting mass concentration of the ferria sol was 2%.

2.3. Alumina hydrosol

Stable alumina hydrosol was prepared using a processing route described in our previous work (Chapurina et al., 2016) and illustrated in Scheme 1b. 3.3 g of aluminum isopropoxide was added to 100 ml of deionized water pre-heated to 80 °C under constant stirring (300 rpm) for 10 min. Then, the resulting suspension was subjected to ultrasonic treatment (37 kHz,
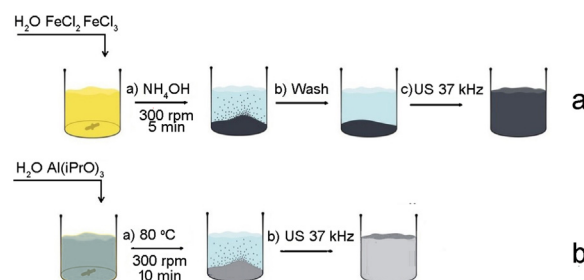
Scheme 1 Preparation routes of ferria (a) and alumina (b) hydrosols.

110 W) under constant stirring (300 rpm). The resulting boehmite sol was afterwards cooled to room temperature. The resulting mass concentration of the alumina sol was 2%.

2.4. Ferria-alumina composites

For preparation of composite materials, the freshly prepared ferria hydrosol (0.75–0.25 mL) was mixed with the alumina hydrosol, then the solution was homogenized by vigorous mixing. The prepared solution was dried in an evaporator at 60 °C at normal pressure and the resulting xerogel was ground in a mortar.

2.5. Wastewater

Wastewater sample was taken from rinsing wastewater of degreasing and metal plating process in electroplating laboratory of ITMO University.

2.6. Cr(VI) adsorption and sorbent regeneration

The adsorption isotherms of Cr(VI) ions were studied using 20 mg of the sample dispersed in 10.0 mL bichromate solutions with the initial concentrations of Cr(VI) ions ranging from 10 to 150 mg/L under constant stirring for 60 min. The temperature of adsorption was 25 °C and the pH values of the initial Cr(VI) solutions were 2.0 ± 0.1. After the experiments, the suspensions were filtered through membrane filters with a pore size of 0.2 m and Cr(VI) concentrations in the filtrate was determined by the 1,5-diphenylcarbazide method (Farag et al., 1981). For regeneration, adsorbents were stirred in 20 mL of NaOH (0.005 M) at 25 °C for 30 min. The nanoparticles were magnetically separated, washed with deionized water and reused in the experiments.

2.7. Adsorbent stability

In order to evaluate the stability of the materials, aluminium and iron leaching were measured by atomic absorption spectroscopy. For this purpose the materials were incubated at pH 2 or pH 12 for 10 h at 25 °C under constant stirring, then the supernatant was analyzed using standard procedures (Centi et al., 2000; Strohmeier and Hercules, 1984).
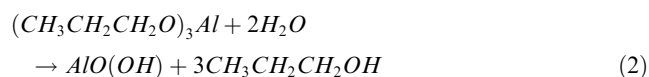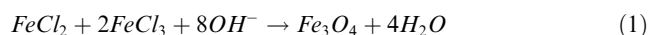
2.8. Characterization methods

Surface area, pore volume, and pore size distributions were investigated by the nitrogen adsorption technique at 77 K using Quantachrome Nova 1200e and subsequent analysis by BET and BJH methods. Prior to analysis, all samples were degassed at 110 °C for 4 h. The particle size distribution and zeta potential were measured using a Photocor Compact-Z analyzer. The crystalline phase and crystallinity of the samples were characterized by X-ray diffraction (Bruker D8 Advance) using Cu $K\alpha$ radiation ($\lambda = 1.5418$ Å). The particle morphology and size were investigated by scanning electron microscopy (SEM) using a VEGA3 TESCAN scanning electron microscope equipped with an X-Act EDX detector. The Raman spectra were recorded using the 633 nm He-Ne laser line on a Horiba Jobin-Yvon Micro Raman 300 spectrometer.

The laser power on the samples employed was 0.030 mW and 0.344 mW, with 300 s and 120 s exposition per diffraction window, respectively. In all the measurements, $50\times$ Olympus lens, hole of 500 mm, slit of 100 mm and a diffraction grid with 1800 grooves/mm were employed. The samples for transmission electron microscopy (TEM) were obtained by dispersing a small probe in ethanol to form a homogeneous suspension. Then, the suspension was drop-coated on a copper mesh covered with carbon for a TEM analysis (FEI TECNAI G2 F20, at an operating voltage of 200 kV). Spectrophotometry was carried out using an Agilent Cary HP 8454 Diode Array spectrophotometer with TEC. Atomic adsorption spectroscopy was performed using Perkin-Elmer Model 2380 AAS.

3. Results and discussion

3.1. Ferria and alumina hydrosols

The synthesis of ferria-alumina composites was performed in three stages: synthesis of magnetite hydrosol, synthesis of alumina hydrosol, and room temperature sol-gel transition. The synthesis of magnetite hydrosol was performed by the modified coprecipitation route. While the mechanism of the reaction is complex and may involve multiple intermediary products, the overall reaction can be described by Eq. (1) resulting in the formation of truncated octahedral nanoparticles of magnetite (Ahn et al., 2012). The formation of boehmite in the present investigation can be envisaged by the hydrolysis and alcohol condensation reaction as demonstrated in Eq. (2):

$$FeCl_2 + 2FeCl_3 + 8OH^- \rightarrow Fe_3O_4 + 4H_2O \tag{1}$$

$$(CH_3CH_2CH_2O)_3Al + 2H_2O$$
$$\rightarrow AlO(OH) + 3CH_3CH_2CH_2OH \tag{2}$$

The results of material characterization for the both hydrosols are illustrated in Fig. 1(a-h). The hydrosols were obtained in form of jelly-like fluids, remaining stable without precipitation for a long period (Fig. 1a, e). Analysis of their hydrodynamic parameters showed narrow particle size distributions with an average hydrodynamic diameter of 74 and 32 nm for boehmite and magnetite, correspondingly. The high stability of the hydrosols was evidenced by highly positive zeta-potential values of the nanoparticles (NPs): $+42$ mV at pH 7.0 and $+36$ mV at pH $= 7.4$ in the alumina and ferria hydrosols, correspondingly. The enhanced hydrosols stability was assisted by application of ultrasonic (US) irradiation in a course of synthesis, thus improving the hydrophilic properties of the synthesized nanoparticles. Acoustic cavitation caused by US-irradiation leads to formation, growth, and implosive collapse of bubbles at the liquid-solid interface (Prosperetti and Plesset, 1978). The implosive collapse of bubbles generates local heating of the contact area through the adiabatic compression or formation of a shock wave in the gas phase of a bubble, whose speed can reach 100 m/s. This results in instantaneous heating of the particle surface and bordering water layer. Under such circumstances, free radicals such as H· and OH· can form and interact with the surface of colloidal particles, resulting in the surface hydroxylation and shifting the isoelectric point of the materials to higher values. The experimentally observed shifts ranged from pH $= 8.3$ to pH $= 10$ for the boehmite NPs and from pH $= 6.8$ to
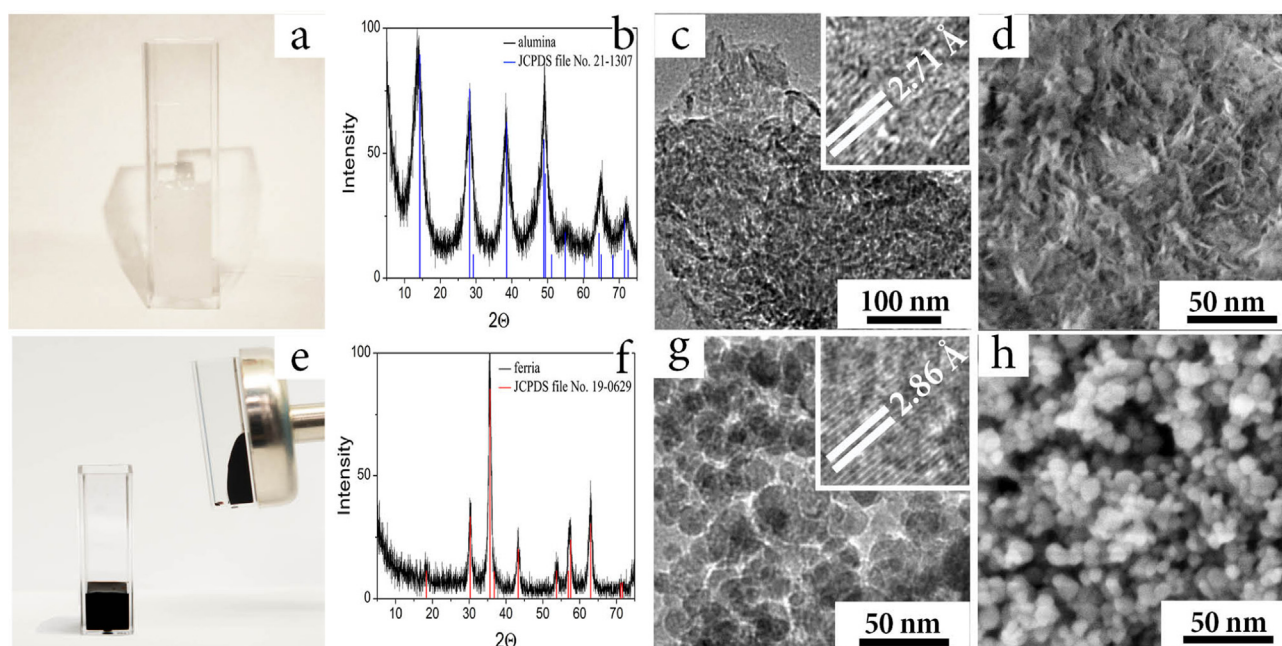
Fig. 1 Alumina (a-d) and ferria (e-h) hydrosols used for preparation of the composites. Visual appearance of the as-synthesized alumina (a) and ferria (e); XRD spectra of the alumina, (reference JCPDS 21-1307 shown as the blue lines) (b), and ferria (reference JCPDS No. 19-0629 shown as red lines) (f); HR-TEM image of the alumina (c) and ferria (g) samples, interplanar spaces are shown in the inserts; HR-SEM image of alumina (d) and ferria (h).

pH = 8.0 for the magnetite NPs (ESI Fig. 1S). Thus the highly positive values of the NPs zeta-potential were achieved even at neutral pH levels and led to the formation of stable hydrosols of alumina and ferria (Fig. 1a, e).

The alumina hydrosol consisted of nanoparticles with an average crystallite size of $5 \times 5 \times 2$ nm according to TEM and SEM (Fig. 1c, d). Clear visibility of lattice fringes (width = 0.271 nm) in Fig. 1c confirms the crystalline nanoparticle structure. XRD patterns (Fig. 1 of the as-synthesized nanoparticles demonstrated broad peaks, indicating ultra-fine and small crystallite sizes and matched with the XRD pattern for boehmite crystalline phase (reference JCPDS 21-1307). The main peak at 14.45° is attributed to the crystalline plane with Miller indices of (0 2 0). Other distinctive peaks at 28.10° (1 2 0), 38.38° (0 3 1), 49.09° (0 5 1), 54.98° (1 5 1), 64.62° (0 2 2), 71.99° (2 5 1) (Fig. 1b) are matched those of the standard boehmite diffraction pattern (Xia et al., 2013). Cell parameters of 2.824 (a), 12.481 (b) and 3.689 (c) agree with the reference values for boehmite crystal phase (Xia et al., 2013). Analysis of the hydrosol hydrodynamic parameters by the dynamic light scattering technique showed narrow size distribution of particles with an average hydrodynamic diameter of 74 nm. Having the zeta-potential value of $+42$ mV at pH 7.0, the synthesized boehmite nanoparticles formed a jelly-like hydrosol that remained stable without precipitation for a long period (Fig. 1a).

In its turn, the ferria hydrosol consisted of nanoparticles with an average mean particle diameter of 10 ± 2 nm and truncated octahedron morphology according to TEM (Fig. 1g) and SEM (Fig. 1h) images. XRD pattern of the nanoparticles corresponded to magnetite crystalline phase (JCPDS No. 19-0629) and demonstrated the main peak at 35.45° attributed to the crystalline plane with Miller indices

of (3 1 1). Other distinctive peaks at 18.52° (0 2 0), 30.10° (2 2 0), 43.08° (4 0 0), 53.45° (4 2 2), 56.98° (5 1 1), 62.57° (4 4 0), 70.99° (5 3 3), and 74.02° (4 4 4) (Fig. 1f) matching the standard magnetite diffraction pattern (Cornell and Schwertmann, 2003). Measured lattice spacing d values of 0.297, 0.253, 0.209, 0.161, and 0.148 nm was agreed with the reference values of 0.297, 0.253, 0.209, 0.162, and 0.149 nm for the (2 2 0), (3 1 1), (4 0 0), (5 1 1), and (4 4 0) crystallographic planes of Fe_3O_4, respectively (Cornell and Schwertmann, 2003). This confirmed the inverse spinal structure of the synthesized ferria nanoparticles (space group $Fd3m$) with the lattice parameter $a = 0.8370$ nm that correlates with the one provided in JCPDS file No. 19-0629. Fig. 2 illustrates the Raman spectra of the magnetite sample recorded in batch experiments at different laser beam powers. It demonstrates an additional evidence of the magnetite crystal phase in the synthesized materials. The line (a) in Fig. 2 was recorded at a 633 nm He-Ne laser power of 0.030 mW with acquisition time of 300 s per diffraction window. It shows the characteristic broad band, typical for magnetite at 667 cm[1] (Li et al., 2012). Further observations have been in agreement with the known series of phase transformations of magnetite under the Raman laser measurement conditions: as the power was increased to 0.344 and 1.35 mW (acquisition times of 90 and 30 s, respectively), the characteristic maghemite bands were observed at 711, 492, and 372 cm^{-1} (Fig. 2 line b), and finally, the full oxidation state was characterized by the hematite characteristic bands at 591, 385, 273, and 213 cm^{-1} (Fig. 2 line c) (Li et al., 2012; Andreeva et al., 2017).

Fig. 3 illustrates the magnetic attraction of the mixed hydrosols with various alumina to ferria ratios. As the ferria mass fraction decreases, the attraction of the hydrosol to the magnet is weakening. Due to high zeta potential ($+36$ mV at
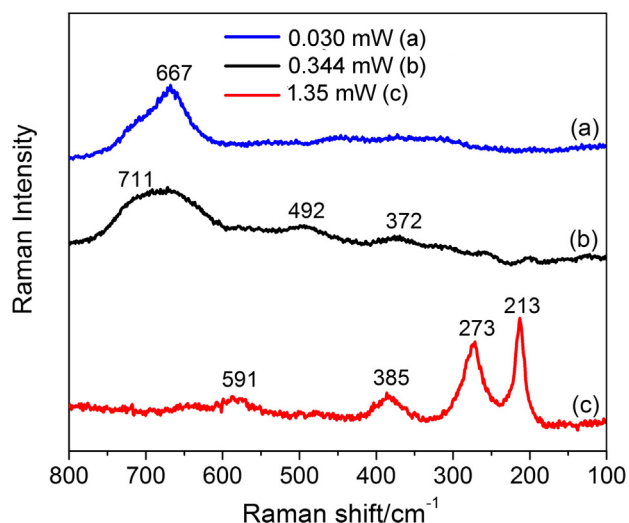
Fig. 2 Raman spectra of the magnetite sample recorded in batch experiments at different laser beam powers.

pH = 7.4), the magnetite nanoparticles formed stable hydrosol with magnetic fluid-like behavior (Fig. 1e). As shown in Fig. 3, they can be attracted by an external magnetic field together with the dispersion phase (Fig. 3). Since the alumina particles in the mixed hydrosols have similar charge as ferria, these two oxides can be mixed at any ratio without mutual destabilization, thus ensuring a high degree of the colloidal homogeneity of the resulting solution (Fig. 3). The colloidal stability of the blends appeared to be high enough to prevent any notable precipitation during one week of storage on the shelf. The stability of the ferria-alumina blends are close to one observed for pure ferria and alumina hydrosols described earlier (Drozdov et al., 2016; Chapurina et al., 2016) and is thus a distinctive feature of the materials prepared by US-assisted synthesis (Vinogradov and Vinogradov, 2014; Kwan et al., 2015; Gedanken, 2007).

3.2. Ferria-alumina sol-gel derived matrices

One of the main features of the synthesized hydrosols is a pristine surface of NPs in the colloidal solution. Their surfaces shall be free of organic molecules or peptizing agents in order to take part in sol-gel process. Upon solvent removal, the synthesized hydrosols transform into mesoporous xerogel matrices with the controllable alumina-to-ferria ratio. All the observed sol-gel transitions were irreversible and resulted in stable ceramic matrices not inclined to spontaneous re-dispersion in water media. The TEM and SEM analyzes showed a uniform distribution of the components in the resulting materials (Fig. 4a-c). The homogeneous coloring of the energy-dispersive X-ray mapping (Fig. 4b) indicates the absence of aggregation that might have occurred at some critical processing stages such as mixing or solvent removal. Such uniform distribution of components in the sol-gel derived materials is a distinctive feature of sol-gel processes performed with highly homogeneous systems prior to gelation (Tabesh et al., 2018; Drozdov et al., 2016; Nassar et al., 2017). The XRD spectra of the composites include the series of peaks associated with their both components (reference JCPDS files 19-0629 and 21-1307), thus proving their presence in crystal form (Fig. 4d-f).

In order to investigate the nature of interactions between magnetite and boehmite nanoparticles in the ferria-alumina composites, a sample of (1:1) was investigated with Raman spectroscopy. All the observed reflections can be attributed to the characteristic peaks of pure magnetite (667 cm^{-1}) and boehmite (684, 497, 462, 362, 338 cm^{-1}) while no any additional vibrational modes corresponding to potential Fe-O-Al bonds were observed. (see ESI Fig. 2S) This suggests no chemical interaction between boehmite and magnetite occurred during the sol-gel processing. Thus the derived materials can be described as two interlaced sol-gel matrices rather than monolithic ceramic material. The textural properties of the formed xerogels are shown in Fig. 5(a-c). The surface areas of pure
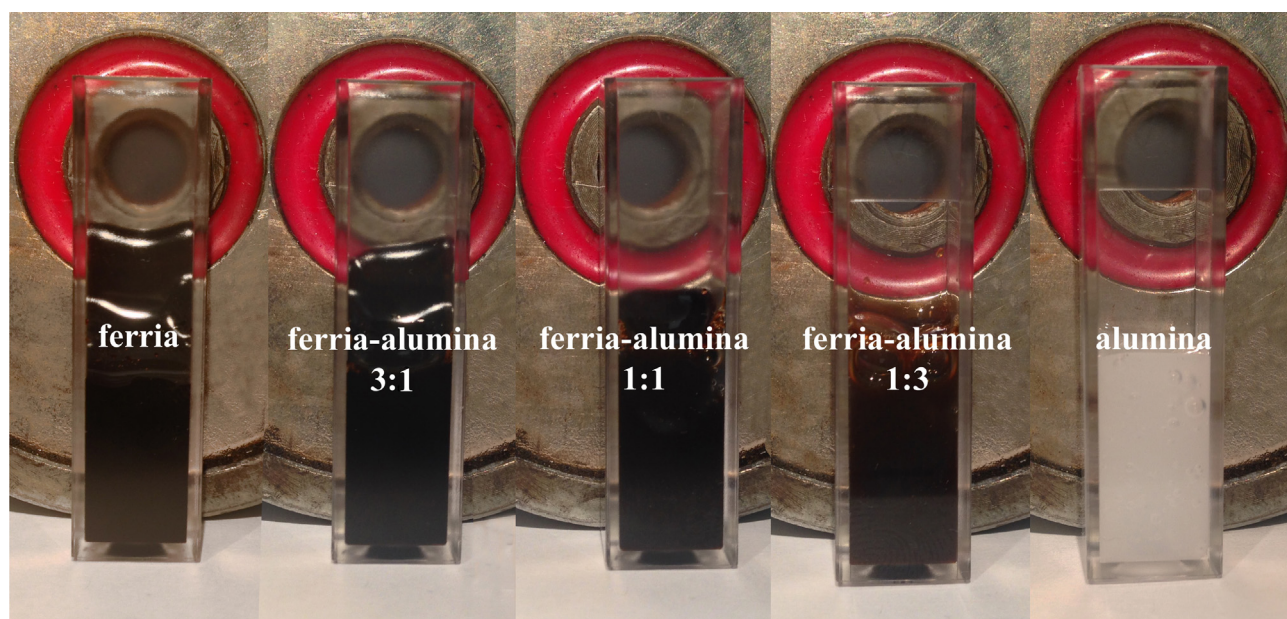

Fig. 3 Visual appearance of ferria and alumina hydrosols and their mixtures.
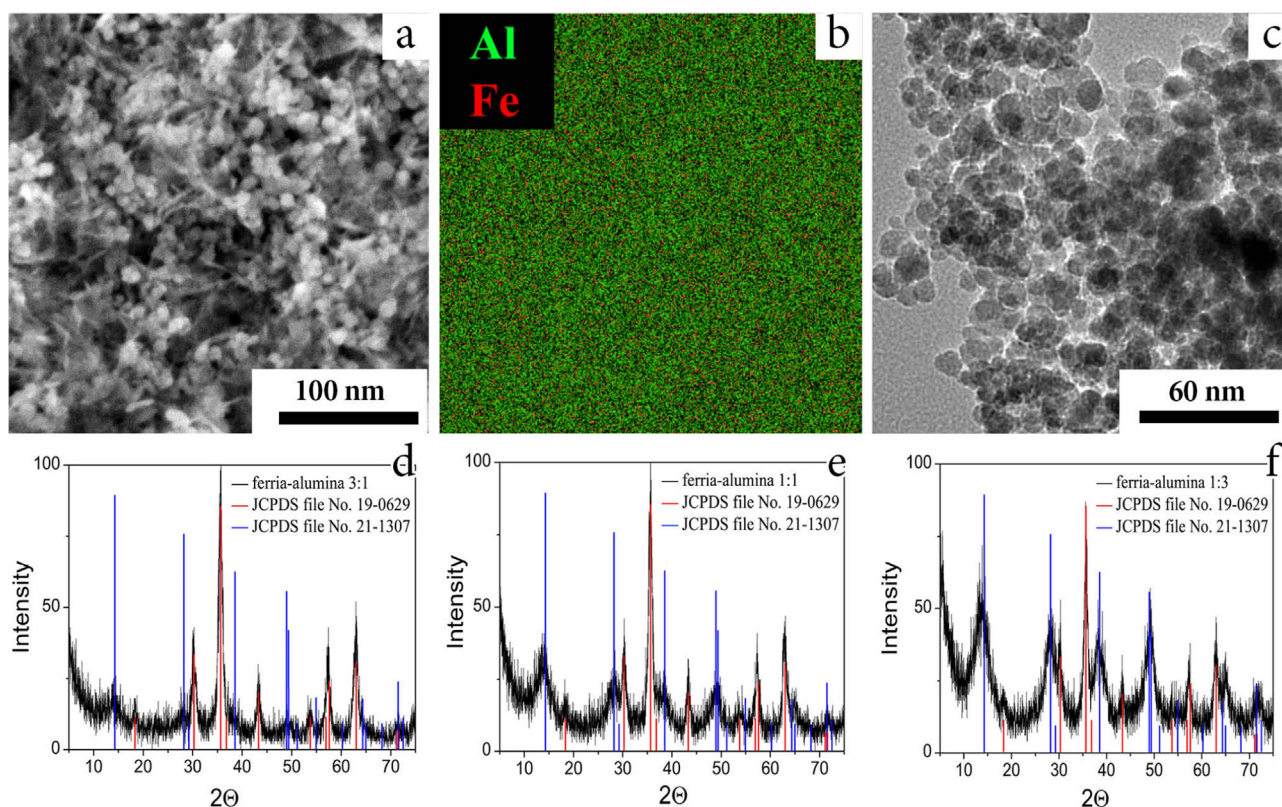
Fig. 4 Characterization of composite matrices. HR-SEM image of the ferria-alumina 1:1 composite (a); EDX image of the ferria-alumina 1:1 composites (b); TEM image of the ferria-alumina 1:1 composite (c); XRD spectra of the ferria-alumina composite with mass fractions ferria-alumina varied from 3:1 to 1:3, respectively (d-f).
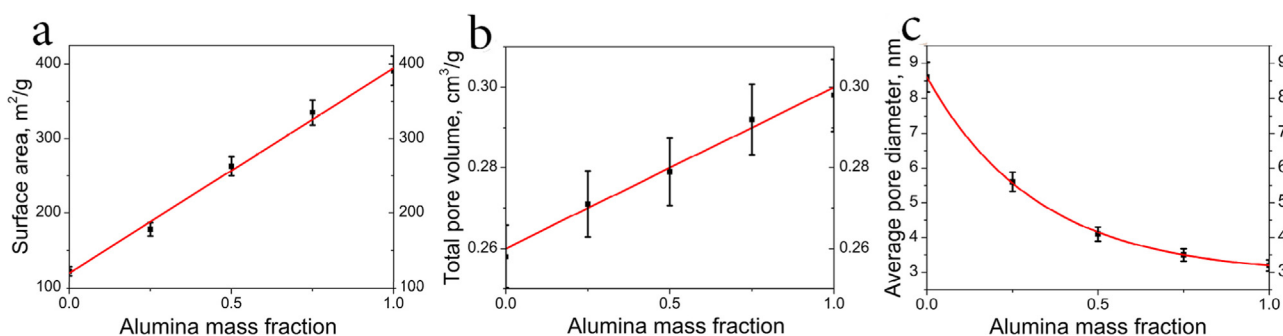

Fig. 5 Textural properties of the composite materials. Surface area as a function of the alumina mass fraction (a); total pore volume as a function of the alumina mass fraction (b); average pore diameter as a function of the alumina mass fraction (c).

magnetite and boehmite xerogels were determined as 122 m^2/g and 391 m^2/g, respectively, as well as their linearly depending ratios in the intermediate composites (Fig. 5a). The total pore volume in the materials also demonstrated a linear increment ranging from 0.258 cm^3/g in pure ferria to 0.298 cm^3/g in pure alumina xerogels (Fig. 5b). The average pore diameter demonstrated an exponential decay with an increase of alumina mass fraction (Fig. 5c). This can be a result of the two factors. First, the smaller average size of the boehmite nanoparticles favors smaller average pore diameter. Second, the difference in morphology of the nanoparticles (flakes of alumina, Fig. 1c, and truncated tetrahedrons of ferria, Fig. 1g) results in more dense

packing of the materials with higher alumina content. The zeta potential of composite materials depends on alumina mass fraction and linearly increases from +18 to +24 mV while moving from pure ferria to pure alumina (see ESI Fig. 3S).

The magnetic properties of the synthesized materials have been characterized, and the corresponding magnetization curves measured for several iron containing composites are shown in Fig. 6. All the curves demonstrate superparamagnetic behavior with high saturation magnetization. They do not demonstrate any hysteresis, neither any remnant magnetization. Variation of the magnetite mass fraction is shown to control the amplitude of the magnetization response, up to the
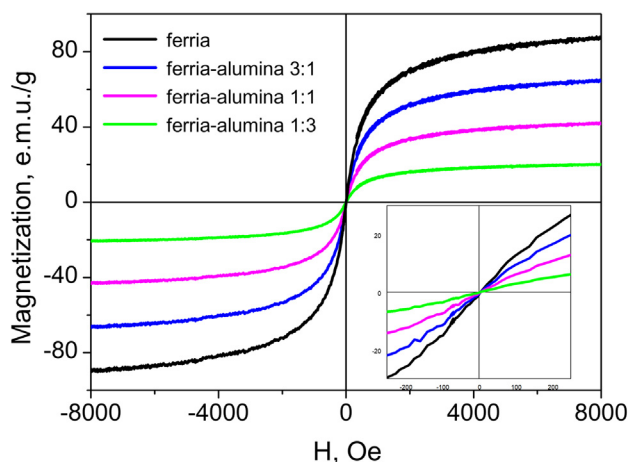
Fig. 6 Magnetization curves of the composite materials. Inset: the low-field.

level of 88 emu/g in the pure ferria, which is close to the value of bulk magnetite ($\approx$92 emu/g) (Mikhaylov et al., 2017). As aluminium and its oxides have very weak paramagnetic properties (with permeability at the level of 10^{-5} H/m), its presence in the composite material do not affect the magnetic behavior of the material, thus the net magnetic properties of the ferria-alumina composites are determined only by the mass fraction of magnetite nanoparticles. All the measured magnetization curves have been analyzed using the Langevin function (Eq. (3)):

$$M = M_s \left[\coth \left(\frac{\mu H}{k_b T} - \frac{k_B T}{\mu H} \right) \right] \quad (3)$$

where M and M_s are the magnetization and saturation magnetization respectively, μ is the magnetic moment, H is the external magnetic field, T is temperature, and k_B the Boltzmann constant. The particle size can be inferred from the Langevin function adjusting the parameter $a = \mu/k_B$, which is related to the particle diameter d as $a = 4\pi(d/2)^{3 *} M_0/3k_B$. The resultant average particle size was found to be 10.5 $\pm$ 0.5 nm for ferria in composite materials. This is in agreement with the values determined by TEM, SEM and XRD methods (Fig. 2).

The high magnetization properties of the ferria-alumina composites can be used for their magnetically controlled separation in various solutions. An optimal balance between the magnetization and textural properties of the functional ferria-alumina composite can thus be adjusted by the ratio between the constituent components to meet the specific requirements of various applications.

3.3. Chromate absorption mechanism

The combination of high surface area and high magnetization makes the ferria-alumina composites promising adsorbent for water purification. In aqueous systems, the surfaces of the both constituent oxides are covered with hydroxyl groups, which could be protonated or deprotonated to generate charged $M\text{-}OH_2^+$ or $M\text{-}O^-$ functional, respectively, groups at pH values below or above the zero point of charge (PZC). In the materials under study the PZC was observed at pH = 8 (for ferria) and pH = 10 (for alumina), thus implying protonation and

positive charging of their surfaces at neutral or acidic media. Adsorption of chromate ions to the surface of magnetite or boehmite is a result of their electrostatic interaction and greatly depends on the pH level of the solution. Thus, the electrostatic adsorption of the chromate anions requires the positive charge of the NPs surface. At low pH, a variety of different Cr-anionic species ($Cr_2O_7^{2-}$, $HCrO_4^-$, $Cr_3O_{10}^{2-}$, $Cr_4O_{13}^{2-}$) may coexist in water (Yuan et al., 2009). In order to ensure the maximal chromium adsorption capacities the corresponding pH level is typically maintained at 2–3, at which the main form of adsorbed chromate species is represented by $HCrO_4^-$ with relatively low adsorption free energy (2.5–0.6 kcal/mol) (Yuan et al., 2009).

Let us now discuss the possible mechanisms of chromium adsorption to ferria and alumina surfaces. Fig. 7 illustrates the different scenarios for adsorption of a chromate ion on the surfaces of ferria (Fig. 7a) and alumina (Fig. 7b). The ferria lattice region contains both Fe^{2+} and Fe^{3+} sites. The surface Fe^{3+} sites are depicted as adsorbing the $HCrO_4^-$ ions (Fig. 7a), although both Fe^{2+} and Fe^{3+} surface sites might be involved. In this case, the chromate ion adsorption typically involves two-site (chelating) bonding to the surface, though the single Fe-O-Cr attachment may also occur. Likewise, $HCrO_4^-$ and CrO_4^{2-} will be in equilibrium in a solution thus both competing to react at the surface site (Rajput et al., 2016). The ratio of Fe^{2+}/Fe^{3+} sites represented in the schemes is obviously arbitrary for these idealized pathways, only suggesting a clue to the mechanism involved. In case of alumina, the adsorption mechanism is more dependent on the pH level of the solution. For pH above 6, the inner-sphere monodentate and bidentate complexes are the dominant pathway for chromate adsorption
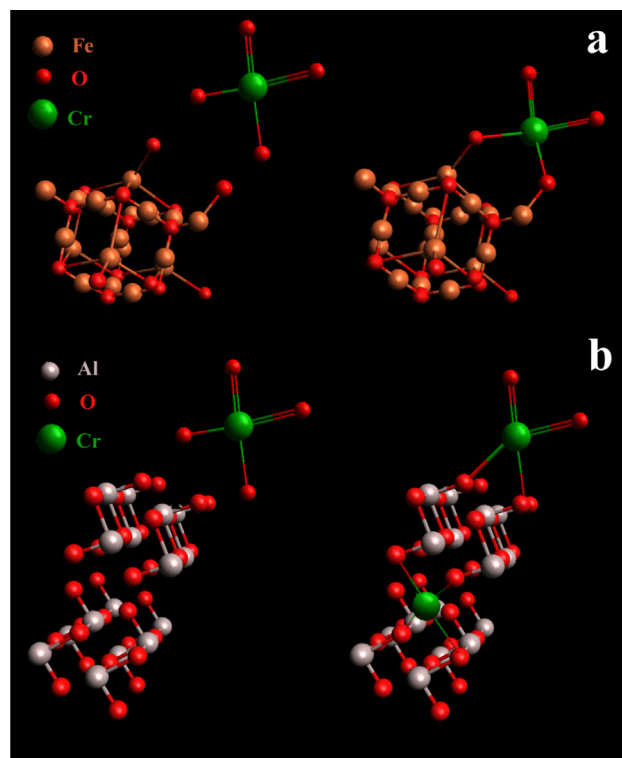

Fig. 7 Adsorption mechanisms for a chromate ion on the ferria (a) and alumina (b) surface.

(Fig. 7b), while for pH ranging between 2 and 3 the outer-sphere complexes are observed. The chromate adsorption is suppressed at pH < 2 and high ionic strength values, because similar reaction mechanisms are responsible for these processes. It is supposed that this suppression is related to limited availability of exchangeable surface groups and those inner-sphere complexes should also be considered (Johnston and Chrysochoou, 2015).

3.4. Chromate absorption kinetic

The adsorption kinetics is one of the key features of the adsorption process, important for both modeling and application purposes. The kinetic curves obtained for several composites with various ferria-to-alumina ratios are shown in Fig. 8. These curves clearly demonstrate that the sorption equilibrium depends on the ferria-to-alumina ratio of the composites. The adsorption equilibrium depends on the total surface area of the sorbent material. For the system under study it increases gradually from 23 mg/g to 62 mg/g with an increase of the alumina fraction in the composite xerogel matrices (Fig. 8a). Plotting the t/q_e ratio versus time (Fig. 8b) yields a set of straight linear dependencies for materials with various ferria-to-alumina ratios, Thus the sorption mechanism can be described by the second-order equation (Rodrigues and da Silva, 2009) Eq. (4):

$$\frac{1}{q_t} = \frac{1}{k_2 q_t^e} + \frac{t}{q_e} \tag{4}$$

where k_2 is the pseudo-second-order rate constant ($h^{-1} * g * mg^{-1}$), t is time, q_t and q_e are the amounts of chromate adsorbed at time and at equilibrium (mg/g).

The adsorption isotherms have been analyzed using the Langmuir and Freundlich equations (Langmuir, 1918; Freundlich, 1906). The Langmuir equation is associated with an isotherm model assuming that (1) the adsorbent surface is homogeneous; (2) adsorption is limited by monomolecular layer coverage; (3) there are no interactions between adsorbate molecules (Langmuir, 1918). The Langmuir equation can be expressed as follows Eq. (5):

$$\frac{C_e}{q_e} = \frac{1}{K_L q_m} + \frac{1}{q_m} * C_e \tag{5}$$

where C_e is the equilibrium Cr(VI) concentration (mg/L), q_e is the equilibrium Cr(VI) sorption capacity (mg/g), q_m is the monolayer capacity (maximum sorption capacity corresponding to the complete filling of the monolayer, mg/g), K_L is the Langmuir constant (adsorption coefficient, which depends on the adsorption energy and temperature, L/mg). An important feature of K_L is its relation to the affinity between the metal ions and the adsorbent. The Freundlich isotherm is an empirical adsorption model adopted for a case of nonhomogeneous adsorbent surface. The Freundlich equation can be expressed as follows (Freundlich, 1906) Eq. (6):

$$\ln q_e = \ln K_F + \frac{1}{n} * \ln C_e \tag{6}$$

where K_F and n are the Freundlich isotherm constants related to adsorption capacity and adsorption strength of the adsorbent, respectively. Parameter K_F represents the adsorption capacity of the material. The slope $1/n$ serves to describe the linearity of adsorption and indicates an extent of the adsorption process to be favorable. The adsorption isotherm parameters and correlation regression coefficients have been calculated using the Langmuir and Freundlich models and summarized in Table 1.

Analysis of the R-squared standard deviations listed in Table 1 suggests that the Langmuir model fits better the experimental data (with R^2 (> 0.941). This is an indication of rather homogeneous distribution of the active sites on the adsorbent surfaces. The $1/n$ values are in the range of 0–1 for all samples, suggesting that the adsorption is thermodynamically favorable. The adsorption capacity of materials gradually increases with an increase of the alumina mass fraction, in correlation with a change in the specific surface area determined by physical nitrogen adsorption. Compared to magnetite-based adsorbents reported in earlier studies, the composite materials demonstrate significantly enhanced sorption capacities (see ESI Table 1S). This can be an effect of larger surface areas and higher saturation of the surface by hydroxyl groups, as
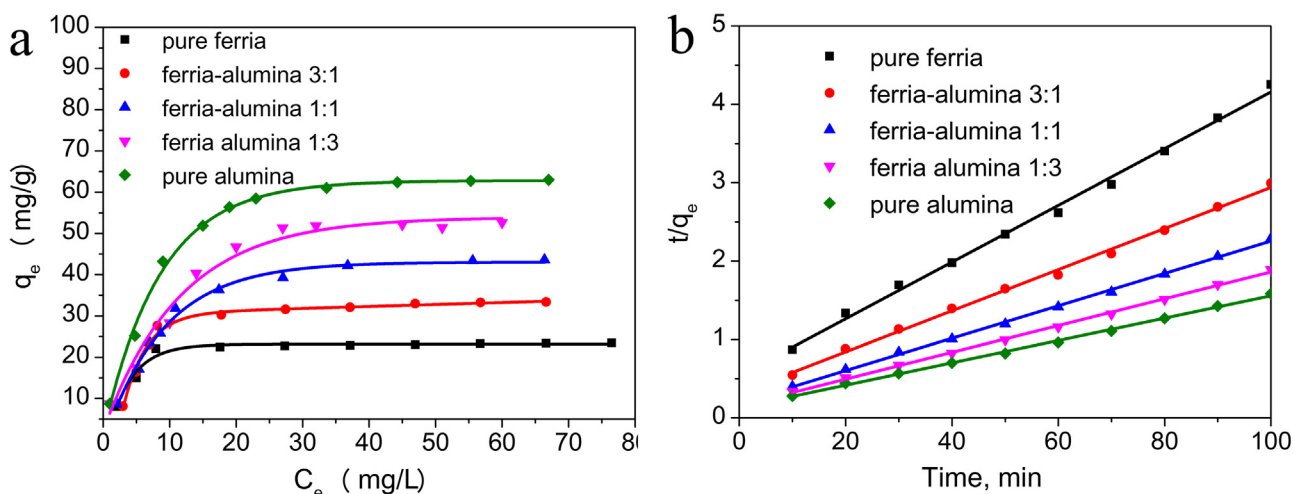

Fig. 8 Adsorption curves of Cr(VI) ions on composite materials. Kinetic curve of the chromate adsorption (a); Pseudo-second-order kinetics curves for the adsorption of Cr(VI) (b).

Table 1 The adsorption isotherm parameters and correlation regression coefficients.

Alumina mass fraction	Langmuir			Freundlich		
	q_m	K_L	R^2	K_F	$1/n$	R^2
0	23.51	22.41	0.951	2.52	0.341	0.854
0.25	22.41	25.97	0.964	2.58	0.364	0.867
0.5	43.65	27.31	0.941	2.74	0.322	0.871
0.75	52.87	30.45	0.971	3.12	0.387	0.837
1	62.41	35.78	0.961	4.51	0.391	0.872

a result of the compositional variation and the applied synthesis conditions.

3.5. Absorbents recycling

As mentioned earlier, the magnetosensitive properties of the composite adsorbents allow performing their magnetic separation with a subsequent regeneration and recycling. In the laboratory experiments this was realized using a permanent magnet, while special flow magnetic separators can be used in real applications, with a performance up to several tons per hour (Yavuz et al., 2009; De Latour, 1973; Rossier et al., 2012). In order to investigate the reuse potential of the composites, the materials were separated magnetically (or by centrifugation for pure alumina) and regenerated in sodium hydroxide solution and subjected to another round of adsorption with totally five batches of adsorption – desorption cycles (Fig. 9). A gradual degradation down to 89–92% of absorption capacity was observed for materials after five cycles, depending on material composition. The degradation rate was slightly higher in composites with higher alumina fraction. This difference in materials regeneration can be attributed to a higher energy of chromate ion adsorption to boehmite crystal structure (ΔG_{ads} −140 kJ/mol) in comparison with adsorption on magnetite (ΔG_{ads} −85 kJ/mol) (Johnston and Chrysochoou, 2015; Suh et al., 2015). Compared to the earlier published results, the recyclability of magnetic ferria-alumina composites are found to possess better regeneration properties than the pristine magnetite- based adsorbents (up to 25% degradation after 2 cycles) (Rajput et al., 2016; Wang et al., 2010) and close
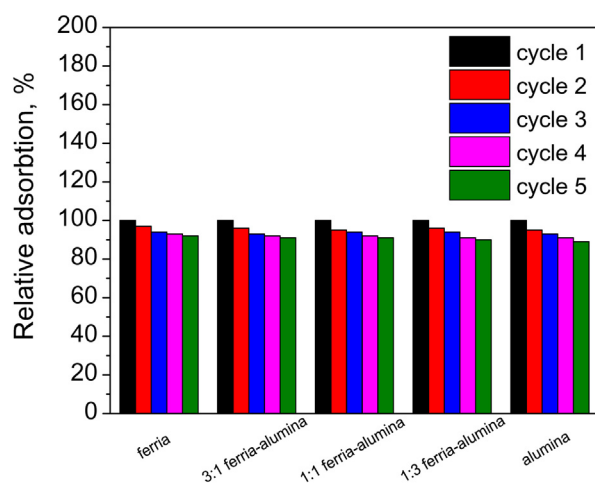
to one observed for magnetite-silica based materials (90–95% of adsorptive capacity regeneration) (Topel et al., 2014; Wang et al., 2010).

In order to further evaluate the prospects of the composites as recyclable adsorbent, their chemical stability was addressed through evaluation of iron and aluminium ions leaching at low (pH 2.0) and high (pH 12.0) conditions for a sufficiently long time period. The composites were found to be stable to bases (leaching of iron and aluminium ions did not exceed 0.1 wt. % after 10 h of incubation for all the tested materials), while notable leaching was observed in acidic media, reaching 12% and 0.5 wt.% for iron and aluminium respectively (for the 3:1 ferria-alumina composite). While this observation implies gradual degradation of the materials, they still can be regenerated and reused for several times until the complete loss of magnetic responsiveness.

3.6. Purification of real wastewater samples

Finally, we address a set of experiments comparing the purification abilities of the designed composites in real conditions. In these experiments we examined them using wastewater obtained after electroplating process. The real wastewater included the following contaminations prior to the experiment: 100 ppm Cr(VI), 21 ppm Al, 25 ppm Mg, 40 ppm Ca, and 10 ppm B. A sample of artificially contaminated water (100 ppm Cr(VI)) was prepared in the laboratory, and used for simulation in similar experiments. The percentage of chromate uptaking by different materials in these experiments is listed in Table 2. In all the cases the purification performance with the simulation liquid was almost 20% higher than with the industrial effluent. Such difference is in agreement with previously published results for other systems and can be attributed

Fig. 9 Recycling of the composite materials.

Table 2 Chromate adsorption in simulated and real wastewater samples by composites.

Material	Removal (%)		Uptake (mg/g)	
	Simulated	Wastewater	Simulated	Wastewater
Ferria	30.6	24.6	23.51	18.92
3:1 ferria-alumina	43.5	34.0	31.41	26.07
1:1 ferria-alumina	56.9	46.0	43.65	35.36
1:3 ferria-alumina	68.9	55.9	52.87	42.91
Alumina	81.3	65.8	62.41	50.51

to the competitive adsorption of interfering ions in the effluent (Dakiky et al., 2002; Martín-Lara et al., 2014).

4. Conclusion

In this article, we presented a simple and cost-efficient processing of the ferria-alumina composite materials based on sol-gel preparation. Composites were produced from stable hydrosols in a course of sol-gel transition under mild conditions and consisted of distinctly crystalline magnetite and boehmite nanoparticles. Combining high magnetization values (up to 88 emu/g) and large surface areas (up to 391 m²/g), the composite materials showed both high chromium sorption capacities (up to 63 mg/g of Cr(VI)) and the ability to be separated by magnetic separation techniques. The adsorption kinetics has been described in terms of the pseudo-second order model. The sorbent properties of ferria-alumina composites have been examined. The multiple regeneration has been demonstrated for the obtained sorbents by washing in NaOH (0.005 M) for at least 5 times, with only 11% adsorption capacity degradation. Inspite of notable leaching of iron ions (up to 12 wt.% after 10 h) was observed at acidic experimental conditions, the materials stability was sufficient for reuse of the composites. The purification examination of the sorbent materials with real electroplating wastewater demonstrated up to 20% decrease of chromate removal efficiency due to competitive adsorption of coexisting ions (Al^{3+}, Mg^{2+}, Ca^{2+}, B^{3+}). Thus the hybrid ferria-alumina nanocomposites may be considered as candidates for sorbent application for purification treatment of chromium contaminated wastewater. The investigated materials revealed themselves as potential recyclable adsorbents for water purification which can be potentially used in real systems for electroplating wastewater treatment. Further research will address improvement of the adsorption capacity in this class of materials via nanoarchitectonic approaches, aiming at broader application variety, including hydrometallurgy and other areas.

Acknowledgements

Appendix A. Supplementary material

Supplementary data associated with this article can be found, in the online version, at https://doi.org/10.1016/j.arabjc.2018.02.011.

References

Abbas, A., Al-Amer, A.M., Laoui, T., Al-Marri, M.J., Nasser, M.S., Khraisheh, M., Atieh, M.A., 2016. Heavy metal removal from aqueous solution by advanced carbon nanotubes: critical review of adsorption applications. Sep. Purif. Technol. 157, 141–161.

Ahmad, M., Ahmed, S., Swami, B.L., Ikram, S., 2015. Adsorption of heavy metal ions: role of chitosan and cellulose for water treatment. Langmuir 79, 109–155.

Ahn, T., Kim, J.H., Yang, H.-M., Lee, J.W., Kim, J.-D., 2012. Formation pathways of magnetite nanoparticles by coprecipitation method. J. Phys. Chem. C 116, 6069–6076.

Aide, M.T., Cummings, M.F., 1997. The influence of PH and phosphorus on the adsorption of chromium (VI) on boehmite. Soil Sci. 162, 599–603.

Andreeva, Y.I., Drozdov, A.S., Fakhardo, A.F., Cheplagin, N.A., Shtil, A.A., Vinogradov, V.V., 2017. The controllable destabilization route for synthesis of low cytotoxic magnetic nanospheres with photonic response. Sci. Rep. 7, 11343.

Calder, L., 1988. Chromium contamination of groundwater. Adv. Environ. Sci. Technol. 20, 215–229.

Camacho, L.M., Torres, A., Saha, D., Deng, S., 2010. Adsorption equilibrium and kinetics of fluoride on sol-gel-derived activated alumina adsorbents. J. Colloid Interface Sci. 349, 307–313.

Centi, G., Perathoner, S., Torre, T., Verduna, M.G., 2000. Catalytic wet oxidation with H_2O_2 of carboxylic acids on homogeneous and heterogeneous Fenton-type catalysts. Catal. Today 55, 61–69.

Chapurina, Y.E., Drozdov, A.S., Popov, I., Vinogradov, V.V., Dudanov, I.P., Vinogradov, V.V., 2016. Streptokinase@ alumina nanoparticles as a promising thrombolytic colloid with prolonged action. J. Mater. Chem. B 4, 5921–5928.

Ciesielczyk, F., Przybysz, M., Zdarta, J., Piasecki, A., Paukszta, D., Jesionowski, T., 2014. The sol-gel approach as a method of synthesis of xMgO· ySiO₂ powder with defined physicochemical properties including crystalline structure. J. Sol-Gel. Sci. Technol. 71, 501–513.

Ciesielczyk, F., Bartczak, P., Klapiszewski, Ł., Jesionowski, T., 2017. Treatment of model and galvanic waste solutions of copper (II) ions using a lignin/inorganic oxide hybrid as an effective sorbent. J. Hazard. Mater. 328, 150–159.

Cornell, R.M., Schwertmann, U., 2003. The Iron Oxides: Structure, Properties, Reactions, Occurrences and Uses. John Wiley & Sons.

Dakiky, M., Khamis, M., Manassra, A., Mer'eb, M., 2002. Selective adsorption of chromium (VI) in industrial wastewater using low-cost abundantly available adsorbents. Adv. Environ. Res. 6, 533–540.

Dayan, A., Paine, A., 2001. Mechanisms of chromium toxicity, carcinogenicity and allergenicity: review of the literature from 1985 to 2000. Hum. Exp. Toxicol. 20, 439–451.

De Latour, C., 1973. Magnetic separation in water pollution control. IEEE Trans. Magn. 9, 314–316.

Deng, S., Nie, Y., Du, Z., Huang, Q., Meng, P., Wang, B., Huang, J., Yu, G., 2015. Enhanced adsorption of perfluorooctane sulfonate and perfluorooctanoate by bamboo-derived granular activated carbon. J. Hazard. Mater. 282, 150–157.

Drozdov, A.S., Shapovalova, O.E., Ivanovski, V., Avnir, D., Vinogradov, V.V., 2016. Entrapment of enzymes within sol-gel-derived magnetite. Chem. Mater. 28, 2248–2253.

Drozdov, A.S., Ivanovski, V., Avnir, D., Vinogradov, V.V., 2016. A universal magnetic ferrofluid: nanomagnetite stable hydrosol with no added dispersants and at neutral pH. J. Colloid Interface Sci. 468, 307–312.

Drozdov, A.S., Vinogradov, V.V., Dudanov, I.P., Vinogradov, V.V., 2016. Leach-proof magnetic thrombolytic nanoparticles and coatings of enhanced activity. Sci. Rep. 6, 28119.

Farag, A., El-Wakil, A., El-Shahawi, M., 1981. Qualitative and semi-quantitative determination of chromium (VI) in aqueous solution using 1, 5-diphenylcarbazide-loaded foam. Analyst 106, 809–812.

Freundlich, H.M.F., 1906. Over the adsorption in solution. J. Phys. Chem 57, 1100–1107.

Gallios, G.P., Tolkou, A.K., Katsoyiannis, I.A., Stefusova, K., Vaclavikova, M., Deliyanni, E.A., 2017. Adsorption of arsenate by nano scaled activated carbon modified by iron and manganese oxides. Sustainability 9, 1684.

Gao, J., Sun, S.-P., Zhu, W.-P., Chung, T.-S., 2014. Chelating polymer modified P84 nanofiltration (NF) hollow fiber membranes for high efficient heavy metal removal. Water Res. 63, 252–261.

Gedanken, A., 2007. Doping nanoparticles into polymers and ceramics using ultrasound radiation. Ultrason. Sonochem. 14, 418–430.

Goyal, R.K., Jayakumar, N., Hashim, M., 2011. Chromium removal by emulsion liquid membrane using [BMIM]+[NTf 2]- as stabilizer and TOMAC as extractant. Desalination 278, 50–56.

Granados-Correa, F., Jiménez-Becerril, J., 2009. Chromium (VI) adsorption on boehmite. J. Hazard. Mater. 162, 1178–1184.

He, H., Xiao, D., He, J., Li, H., He, H., Dai, H., Peng, J., 2014. Preparation of a core–shell magnetic ion-imprinted polymer via a sol-gel process for selective extraction of Cu (II) from herbal medicines. Analyst 139, 2459–2466.

Huang, C., Hu, B., 2008. Silica-coated magnetic nanoparticles modified with γ-mercaptopropyltrimethoxysilane for fast and selective solid phase extraction of trace amounts of Cd, Cu, Hg, and Pb in environmental and biological samples prior to their determination by inductively coupled plasma mass spectrometry. Spectrochim. Acta Part B: Atom. Spectrosc. 63, 437–444.

Idachaba, M.A., Nyavor, K., Egiebor, N.O., 2004. The leaching of chromium from cement-based waste form via a predominantly biological mechanism. Adv. Environ. Res. 8, 483–491.

Ihsanullah, Al-Khaldi, F.A., Abu-Sharkh, B., Abulkibash, A.M., Qureshi, M.I., Laoui, T., Atieh, M.A., 2016. Effect of acid modification on adsorption of hexavalent chromium (Cr (VI)) from aqueous solution by activated carbon and carbon nanotubes. Desalinat. Water Treatm. 57, 7232–7244.

Johnston, C.P., Chrysochoou, M., 2015. Mechanisms of chromate adsorption on boehmite. J. Hazard. Mater. 281, 56–63.

Karimi, M.A., Kafi, M., 2015. Removal, preconcentration and determination of Ni (II) from different environmental samples using modified magnetite nanoparticles prior to flame atomic absorption spectrometry. Arab. J. Chem. 8, 812–820.

Keyhanian, F., Shariati, S., Faraji, M., Hesabi, M., 2016. Magnetite nanoparticles with surface modification for removal of methyl violet from aqueous solutions. Arab. J. Chem. 9, S348–S354.

Kozlowski, C.A., Walkowiak, W., 2002. Removal of chromium (VI) from aqueous solutions by polymer inclusion membranes. Water Res. 36, 4870–4876.

Krivoshapkin, P., Mikhaylov, V., Krivoshapkina, E., Zaikovskii, V., Melgunov, M., Stalugin, V., 2015. Mesoporous Fe–alumina films prepared via sol-gel route. Microporous Mesoporous Mater. 204, 276–281.

Kwan, J., Graham, S., Myers, R., Carlisle, R., Stride, E., Coussios, C., 2015. Ultrasound-induced inertial cavitation from gas-stabilizing nanoparticles. Phys. Rev. E 92, 023019.

Lakshmipathiraj, P., Raju, G.B., Basariya, M.R., Parvathy, S., Prabhakar, S., 2008. Removal of Cr (VI) by electrochemical reduction. Sep. Purif. Technol. 60, 96–102.

Langmuir, I., 1918. The adsorption of gases on plane surfaces of glass, mica and platinum. J. Am. Chem. Soc. 40, 1361–1403.

Legaria, E.P., Topel, S.D., Kessler, V.G., Seisenbaeva, G.A., 2015. Molecular insights into the selective action of a magnetically removable complexone-grafted adsorbent. Dalton Trans. 44, 1273–1282.

Li, Y.-S., Church, J.S., Woodhead, A.L., 2012. Infrared and Raman spectroscopic studies on iron oxide magnetic nano-particles and their surface modifications. J. Magn. Magn. Mater. 324, 1543–1550.

Liu, S., Mishra, S.B., Zhang, Y., Qi, L., 2017. Uptake of hexavalent chromium in electroplating wastewater by hydrothermally treated and functionalized sand and its sustainable reutilization for glass production. ACS Sustain. Chem. Eng. 5, 1509–1516.

Martín-Lara, M., Blázquez, G., Trujillo, M., Pérez, A., Calero, M., 2014. New treatment of real electroplating wastewater containing heavy metal ions by adsorption onto olive stone. J. Clean. Prod. 81, 120–129.

Mikhaylov, V., Maslennikova, T., Krivoshapkin, P., 2017. Characterization and sorption properties of γ-AlOOH/α-Fe$_2$O$_3$ composite

powders prepared via hydrothermal method. Mater. Chem. Phys. 186, 612–619.

Mikhaylov, V., Krivoshapkina, E., Belyy, V., Krivoshapkin, P., 2017. Synthesis and characterization of sponge-like α-Fe microtubes. Chem. Eng. Sci. 163, 27–30.

Mohan, D., Pittman, C.U., 2006. Activated carbons and low cost adsorbents for remediation of tri-and hexavalent chromium from water. J. Hazard. Mater. 137, 762–811.

Nassar, M.Y., Mohamed, T.Y., Ahmed, I.S., Samir, I., 2017. MgO nanostructure via a sol-gel combustion synthesis method using different fuels: an efficient nano-adsorbent for the removal of some anionic textile dyes. J. Mol. Liq. 225, 730–740.

Ölmez, T., 2009. The optimization of Cr (VI) reduction and removal by electrocoagulation using response surface methodology. J. Hazard. Mater. 162, 1371–1378.

Owlad, M., Aroua, M.K., Daud, W.A.W., Baroutian, S., 2009. Removal of hexavalent chromium-contaminated water and wastewater: a review. Water, Air, Soil Pollut. 200, 59–77.

Pandey, M., Tripathi, B., 2017. Synthesis, characterization and application of zinc oxide nano particles for removal of hexavalent chromium. Res. Chem. Intermed. 43, 121–140.

Pellerin, C., Booker, S.M., 2000. Reflections on hexavalent chromium: health hazards of an industrial heavyweight. Environ. Health Perspect. 108, A402.

Prosperetti, A., Plesset, M.S., 1978. Vapour-bubble growth in a superheated liquid. J. Fluid Mech. 85, 349–368.

Qin, G., McGuire, M.J., Blute, N.K., Seidel, C., Fong, L., 2005. Hexavalent chromium removal by reduction with ferrous sulfate, coagulation, and filtration: a pilot-scale study. Environ. Sci. Technol. 39, 6321–6327.

Qureshi, M.I., Patel, F., Al-Baghli, N., Abussaud, B., Tawabini, B.S., Laoui, T., 2017. A comparative study of raw and metal oxide impregnated carbon nanotubes for the adsorption of hexavalent chromium from aqueous solution. Bioinorgan. Chem. Appl. 2017.

Rajput, S., Pittman Jr, C.U., Mohan, D., 2016. Magnetic magnetite (Fe$_3$O$_4$) nanoparticle synthesis and applications for lead (Pb2+) and chromium (Cr6+) removal from water. J. Colloid Interface Sci. 468, 334–346.

Rodrigues, L.A., da Silva, M.L.C.P., 2009. An investigation of phosphate adsorption from aqueous solution onto hydrous niobium oxide prepared by co-precipitation method. Colloids Surf., A 334, 191–196.

Rossier, M., Schreier, M., Krebs, U., Aeschlimann, B., Fuhrer, R., Zeltner, M., Grass, R.N., Günther, D., Stark, W.J., 2012. Scaling up magnetic filtration and extraction to the ton per hour scale using carbon coated metal nanoparticles. Sep. Purif. Technol. 96, 68–74.

Saha, R., Nandi, R., Saha, B., 2011. Sources and toxicity of hexavalent chromium. J. Coord. Chem. 64, 1782–1806.

Shabanova, E.M., Drozdov, A.S., Ivanovski, V., Suvorova, I.I., Vinogradov, V.V., 2016. Collagenase@ magnetite: proteolytic composite for magnetically targeted minimally invasive surgery. RSC Adv. 6, 84354–84362.

Song, B., Zeng, G., Gong, J., Liang, J., Xu, P., Liu, Z., Zhang, Y., Zhang, C., Cheng, M., Liu, Y., 2017a. Evaluation methods for assessing effectiveness of in situ remediation of soil and sediment contaminated with organic pollutants and heavy metals. Environ. Int. 105, 43–55.

Song, B., Zeng, G., Gong, J., Zhang, P., Deng, J., Deng, C., Yan, J., Xu, P., Lai, C., Zhang, C., 2017b. Effect of multi-walled carbon nanotubes on phytotoxicity of sediments contaminated by phenanthrene and cadmium. Chemosphere 172, 449–458.

Strohmeier, B.R., Hercules, D.M., 1984. Surface spectroscopic characterization of manganese/aluminum oxide catalysts. J. Phys. Chem. 88, 4922–4929.

Suh, Y.J., Chae, J.W., Jang, H.D., Cho, K., 2015. Role of chemical hardness in the adsorption of hexavalent chromium species onto metal oxide nanoparticles. Chem. Eng. J. 273, 401–405.

Sun, J., Huang, J.-C., 2002. Co-removal of hexavalent chromium during copper precipitation. Water Sci. Technol. 46, 413–419.

Tabesh, S., Davar, F., Loghman-Estarki, M.R., 2018. Preparation of γ-Al_2O_3 nanoparticles using modified sol-gel method and its use for the adsorption of lead and cadmium ions. J. Alloy. Compd. 730, 441–449.

Topel, S.D., Legaria, E.P., Tiseanu, C., Rocha, J., Nedelec, J.-M., Kessler, V.G., Seisenbaeva, G.A., 2014. Hybrid silica nanoparticles for sequestration and luminescence detection of trivalent rare-earth ions (Dy3 + and Nd3 +) in solution. J. Nanoparticle Res. 16, 2783.

Uysal, M., Ar, I., 2007. Removal of Cr (VI) from industrial wastewaters by adsorption: Part I: determination of optimum conditions. J. Hazard. Mater. 149, 482–491.

Vinogradov, A.V., Vinogradov, V.V., 2014. Low-temperature sol-gel synthesis of crystalline materials. RSC Adv. 4, 45903–45919.

Wang, J., Zheng, S., Shao, Y., Liu, J., Xu, Z., Zhu, D., 2010. Amino-functionalized Fe_3O_4@ SiO_2 core–shell magnetic nanomaterial as a novel adsorbent for aqueous heavy metals removal. J. Colloid Interface Sci. 349, 293–299.

Wang, J., Li, Y., Chen, W., Peng, J., Hu, J., Chen, Z., Wen, T., Lu, S., Chen, Y., Hayat, T., 2017. The rapid coagulation of graphene oxide on La-doped layered double hydroxides. Chem. Eng. J. 309, 445–453.

Wang, X., Wang, Y., Hou, H., Wang, J., Hao, C., 2017a. Ultrasonic method to synthesize glucan-g-poly (acrylic acid)/sodium lignosulfonate hydrogels and studies of their adsorption of Cu2 + from aqueous solution. ACS Sustain. Chem. Eng. 5, 6438–6446.

Wang, J., Liang, Y., Jin, Q., Hou, J., Liu, B., Li, X., Chen, W., Hayat, T., Alsaedi, A., Wang, X., 2017b. Simultaneous removal of graphene oxide and chromium (VI) on the rare earth doped titanium dioxide coated carbon sphere composites. ACS Sustain. Chem. Eng.

World Health Organization, 2004. Guidelines for Drinking-water Quality: Recommendations, vol. 1. WHO, Geneva.

Wu, P., Li, S., Ju, L., Zhu, N., Wu, J., Li, P., Dang, Z., 2012. Mechanism of the reduction of hexavalent chromium by organo-montmorillonite supported iron nanoparticles. J. Hazard. Mater. 219, 283–288.

Xia, Y., Jiao, X., Liu, Y., Chen, D., Zhang, L., Qin, Z., 2013. Study of the formation mechanism of boehmite with different morphology upon surface hydroxyls and adsorption of chloride ions. J. Phys. Chem. C 117, 15279–15286.

Yang, X., Erickson, L.E., Hohn, K.L., Jeevanandam, P., Klabunde, K.J., 2006. Sol- Gel Cu- Al_2O_3 adsorbents for selective adsorption of thiophene out of hydrocarbon. Ind. Eng. Chem. Res. 45, 6169–6174.

Yao, W., Wang, J., Wang, P., Wang, X., Yu, S., Zou, Y., Hou, J., Hayat, T., Alsaedi, A., Wang, X., 2017. Synergistic coagulation of GO and secondary adsorption of heavy metal ions on Ca/Al layered double hydroxides. Environ. Pollut. 229, 827–836.

Yavuz, C.T., Prakash, A., Mayo, J., Colvin, V.L., 2009. Magnetic separations: from steel plants to biotechnology. Chem. Eng. Sci. 64, 2510–2521.

Yuan, P., Fan, M., Yang, D., He, H., Liu, D., Yuan, A., Zhu, J., Chen, T., 2009. Montmorillonite-supported magnetite nanoparticles for the removal of hexavalent chromium [Cr (VI)] from aqueous solutions. J. Hazard. Mater. 166, 821–829.

Zeng, M., Huang, Y., Zhang, S., Qin, S., Li, J., Xu, J., 2014. Removal of uranium (VI) from aqueous solution by magnetic yolk–shell iron oxide@ magnesium silicate microspheres. RSC Adv. 4, 5021–5029.

Zhang, Z., Zhang, L., Chen, L., Chen, L., Wan, Q.-H., 2006. Synthesis of novel porous magnetic silica microspheres as adsorbents for isolation of genomic DNA. Biotechnol. Prog. 22, 514–518.

Zhang, J., Zhai, S., Li, S., Xiao, Z., Song, Y., An, Q., Tian, G., 2013. Pb (II) removal of Fe_3O_4@ SiO_2–NH_2 core–shell nanomaterials prepared via a controllable sol-gel process. Chem. Eng. J. 215, 461–471.

Zhu, K., Chen, C., Xu, H., Gao, Y., Tan, X., Alsaedi, A., Hayat, T., 2017. Cr (VI) reduction and immobilization by core-double-shell structured magnetic polydopamine@ zeolitic idazolate frameworks-8 microspheres. ACS Sustain. Chem. Eng. 5, 6795–6802.